Extended “orbital molecules” and magnetic phase separation in $Bi_{0.68}Ca_{0.32}MnO_3$

Fabio Orlandi,[1,*] Arianna Lanza,[2] Riccardo Cabassi,[3] Dmitry D. Khalyavin,[1] Pascal Manuel,[1]
Massimo Solzi,[4] Mauro Gemmi,[2] and Lara Righi[3,5]
[1]*ISIS Facility, Rutherford Appleton Laboratory–STFC, OX11 0QX, Chilton, Didcot, United Kingdom*
[2]*Center for Nanotechnology Innovation @NEST, Istituto Italiano di Tecnologia, Piazza San Silvestro 12, 56127 Pisa, Italy*
[3]*IMEM-CNR, Parco Area delle Scienze 37/A, 43124 Parma, Italy*
[4]*Department of Mathematical, Physical and Computer Sciences, University of Parma, Parco Area delle Scienze 7/A, Parma, Italy*
[5]*Department of Chemistry, Life Sciences and Environmental Sustainability, University of Parma,*
Parco Area delle Scienze 17/A, 43124 Parma, Italy

(Received 8 January 2021; revised 24 February 2021; accepted 24 February 2021; published 19 March 2021)

The low-temperature structure of $Bi_{0.68}Ca_{0.32}MnO_3$ has been solved from electron and neutron diffraction data. The quantitative simultaneous refinement indicates an ordering of the Mn cations in a “stripe/chess”-like pattern. The ordering is accompanied by the formation of short Mn—Mn distances and the rearrangement of the Mn—O bonds indicating the development of complex extended “orbital molecules.” The primary order parameter breaks inversion symmetry and allows the generation of a spontaneous electrical polarization as the secondary order parameter. The neutron data at low temperature indicate the coexistence of a pseudo-CE long-range-ordered structure with a strongly reduced moment and short-range ferromagnetic correlations. These results indicate an intricate competition between the charge, orbital, and magnetic degrees of freedom and the Bi^{3+} stereoactivity in this manganite system.

DOI: 10.1103/PhysRevB.103.104105

I. INTRODUCTION

Charge-ordering (CO) transitions in metal oxides are symmetry-breaking phenomena controlling some macroscopic properties such as transport [1], superconductivity [2], and even multiferroicity [3]. The first example of such phenomena is the Verwey transition in magnetite (Fe_3O_4) [4–6], in which at $T_V = 120$ K a sharp increase of the resistivity is observed [1]. Although the transition has been known for over 80 years, the crystallographic description of the CO phase represented a lively matter of debate with the formulation of various models [5–9]. Recently, a reliable CO superstructure model was proposed [10], showing the formation of three Fe site units over which the localized electrons are distributed. This linear ferromagnetic units, called trimerons, are also observed in other Fe-based oxides showing CO transitions like $CaFe_3O_5$ [11,12] and Fe_4O_5 [13]. The formation of dimers [14], trimers [10–12], and more complex d-metal clusters [15–17] in solid-state systems, usually referred to as “orbital molecules” [18,19], is a fascinating phenomenon involving the competition of various degrees of freedom, such as charge, orbital, and magnetic ordering [10–12,15–17,19,20].

Manganites are another family of compounds showing CO related to metal-insulator transition. The prototypes of this family are $La_{0.5}Ca_{0.5}MnO_3$ and $Pr_{0.5}Ca_{0.5}MnO_3$ in which the average Mn valence is +3.5, indicating the presence of a nominal 50/50 ratio between Mn^{3+} and Mn^{4+}. From the evaluation of the magnetic structure of these compounds [21], Goodenough proposed a rocksalt ordering of the Mn^{3+} and Mn^{4+} ions and a consequent orbital ordering of the Mn^{3+} dz^2 orbitals in a zigzag fashion [22]. On the basis of this proposed CO model, Radaelli *et al.* interpreted x-ray and neutron powder diffraction data collected on $La_{0.5}Ca_{0.5}MnO_3$ [23]. The complete charge separation was, however, challenged by a neutron single-crystal experiment on $Pr_{0.6}Ca_{0.4}MnO_3$ where a scenario involving the pairing of the Mn site was pictured [24]. In this CO structure, the authors indicate only a partial charge distribution with the Mn ions having fractional valence values $Mn^{+3.5\pm\delta}$. The dimerization of the ferromagnetic Mn pair is ascribed to the formation of Zener polarons [24]. Interestingly, several theoretical works [3,25] have predicted that the CO in manganites might induce a ferroelectric state, but the finite conductivity of the samples has hampered the direct detection of a spontaneous electrical polarization [26,27]. The “partial” charge ordering observed in various manganite systems indicates that the charge degree of freedom is not the only variable to take into account to determine the system ground state. Indeed, orbital ordering and magnetism play a pivotal role, and they can compete with the crystal structure and CO determining particular states as well as phase separation at various length scales [28–30].

The situation became even more interesting in Bi-containing manganites, where it is possible to study the interplay of charge, orbital, and magnetic degrees of freedom with the addition of the Bi^{3+} lone pair distortions [31–37]. The peculiar Bi^{3+} stereoactivity can promote or compete with the stabilization of the Mn^{3+} Jahn-Teller distortions and, as a consequence, can influence CO, orbital ordering, and magnetism [31,32,34,37–39]. This competition

---

[*] Author to whom all correspondence should be addressed: fabio.orlandi@stfc.ac.uk

leads to new unconventional phases with peculiar properties and distortions such as the chiral incommensurate ordering of electrical dipoles [31,37]. It is then interesting to investigate Bi-containing compositions at stability edges of the various degrees of freedom.

The $Bi_{1-x}Ca_xMnO_3$ solid solution has been studied extensively, with a particular focus on the high doping region and around the $x = 0.5$ composition [40–45]. Giot *et al.* [41] have determined the CO structure of an antiferromagnetic $x = 0.4$ sample from single-crystal diffraction data. The reported CO structure crystallizes in the $Pnm2_11'$ symmetry obtained from the parent $Pnma1'$ structure with a modulation vector $q = \frac{1}{2}b^*$, consistent with the Zener polaron scenario observed in $Pr_{0.6}Ca_{0.4}MnO_3$ [24]. On the other side, samples close to the $x = 0$ end member $BiMnO_3$ show a very distorted perovskite structure with ferromagnetic ordering [35,45,46].

Intermediate compositions, between the ferromagnetic state and the CO $x = 0.4$ antiferromagnetic phase [41], show peculiar transport and magnetic properties suggesting a strong competition between the different degrees of freedom [45–47]. The low-temperature structure in this region is still not well understood, with contradicting reports in the literature. García-Muñoz *et al.* [47,48] reported the observation, through electron and powder synchrotron x-ray diffraction, of superstructural reflections that can be indexed with a $2\sqrt{2}a_p \times \sqrt{2}a_p \times 4a_p$ unit cell (where $a_p \approx 3.9$ Å is the simple-cubic perovskite unit cell parameter). The authors suggest the presence of two independent propagation vectors $q_1 = \frac{1}{2}a^*$ and $q_2 = \frac{1}{2}c^*$. Due to the weak character of the superstructure peaks, a quantitative refinement of the CO structure was not possible. At the same time for similar compositions, Giot *et al.* [46] reported the phase coexistence, based on powder neutron diffraction data, between a CO antiferromagnetic phase with $Pnm2_11'$ symmetry (corresponding to the propagation vector q_1) and a ferromagnetic structure with $GdFeO_3$ structure.

For these reasons, we have reinvestigated $Bi_{0.68}Ca_{0.32}MnO_3$ via electron and neutron diffraction measurements. The low-temperature structure has been refined quantitatively and shows an unconventional lattice distribution of the Mn cations leading to a polar state with a clustering of the Mn ions forming complex extended “orbital molecules.” Our three-dimensional (3D) electron diffraction data show the presence of a single modulation vector $q = \frac{1}{2}a^* + \frac{1}{2}c^*$ below the metal-insulator transition. The use of the electron beam allowed us to work on the single domain region, and the 3D electron diffraction geometry [49,50] enabled the collection of high-quality data. Symmetry analysis suggests that the primary CO order parameter induces a spontaneous electrical polarization and the clustering of the Mn sites. Low-temperature neutron data confirmed the magnetic phase separation observed in previous reports [46] between a pseudo-CE structure [21,22] and short-range ferromagnetic correlations.

II. EXPERIMENT

$Bi_{0.68}Ca_{0.32}MnO_3$ was synthesized by a conventional solid-state reaction. Stoichiometric amounts of Bi_2O_3, $CaCO_3$, and Mn_2O_3 were ground and calcined at 1173 K for 6 h. The obtained powder was reground, pressed into pellets, and sintered at 1273 K for 9 h. The phase purity was checked by x-ray powder diffraction by means of a Thermo ARL X’tra diffractometer equipped with Cu $K\alpha$ radiation and a Si(Li) Thermo Electron solid-state detector to eliminate the fluorescence of manganese.

3D electron diffraction (3D ED) data were collected on a Zeiss Libra 120 transmission electron microscope operating at 120 kV and equipped with an omega filter for energy filtered imaging and diffraction and a Nanomegas Digistar P1000 device for precession electron diffraction. The samples were prepared by mild grinding in an agate mortar in isopropanol. After sonication, a drop of the dispersion was deposited on a carbon-coated 300-mesh copper grid. 3D ED data were collected in precession mode [49,51] with a parallel nanobeam of 600 nm, obtained in Köhler illumination by a 19 μm condenser aperture, tilting the crystal manually in steps of 1° and recentering the crystal under the beam after each tilt [50]. The semiaperture of the precession cone was set to 1°. Thanks to the diffraction geometry and to reciprocal space integration due to the beam precession, 3D ED diffraction intensities are close to a kinematic approximation and can be successfully used for *ab initio* structure solution [52]. The covered angular range of the data collection was 114° (115 patterns). The measurements were performed at room temperature and 120 K using a Gatan 626 cryotransfer holder. The data were analyzed using the software PETS for the indexing and integration of the reflections [53].

Time-of-flight neutron diffraction data (TOF-NPD) were collected on the cold neutron WISH diffractometer at the ISIS facility (UK) in a 1.5–200 K temperature range [54]. Rietveld refinements of the neutron and electron diffraction data were performed with the JANA2006 software [55]. The symmetry analysis and mode decomposition of the charge ordered and magnetic structures were conducted with the help of the ISODISTORT and ISOTROPY software [56–58].

Zero-field-cooling (ZFC) and field-cooling-warming (FCW) magnetization measurements were performed on a sintered pellet by means of a SQuID MPMS XL Quantum Design magnetometer in an applied field $H_a = 10$ Oe. The dc electrical resistivity was measured with a two-contact configuration in the temperature range 50–300 K. The sample for the pyrocurrent measurements was obtained on sintered pellets, lapped, and metallized with a 20 nm platinum layer by sputtering to obtain a parallel plate capacitor. Pyroelectric currents were measured using a Keithley 2400 Source Meter Unit for sample poling, and a Keithley electrometer 6517B was adopted to detect the thermal depolarizing electric current [59,60].

III. RESULTS

A. Physical characterization

The resistivity measurement performed on $Bi_{0.68}Ca_{0.32}MnO_3$ is shown in Fig. 1(a). At $T_{CO} \approx 173$ K the system undergoes a metal-insulator transition and the upturn of the conduction activation energy goes from 13 to 135 meV. In the frame of magnetoresistance manganites, such

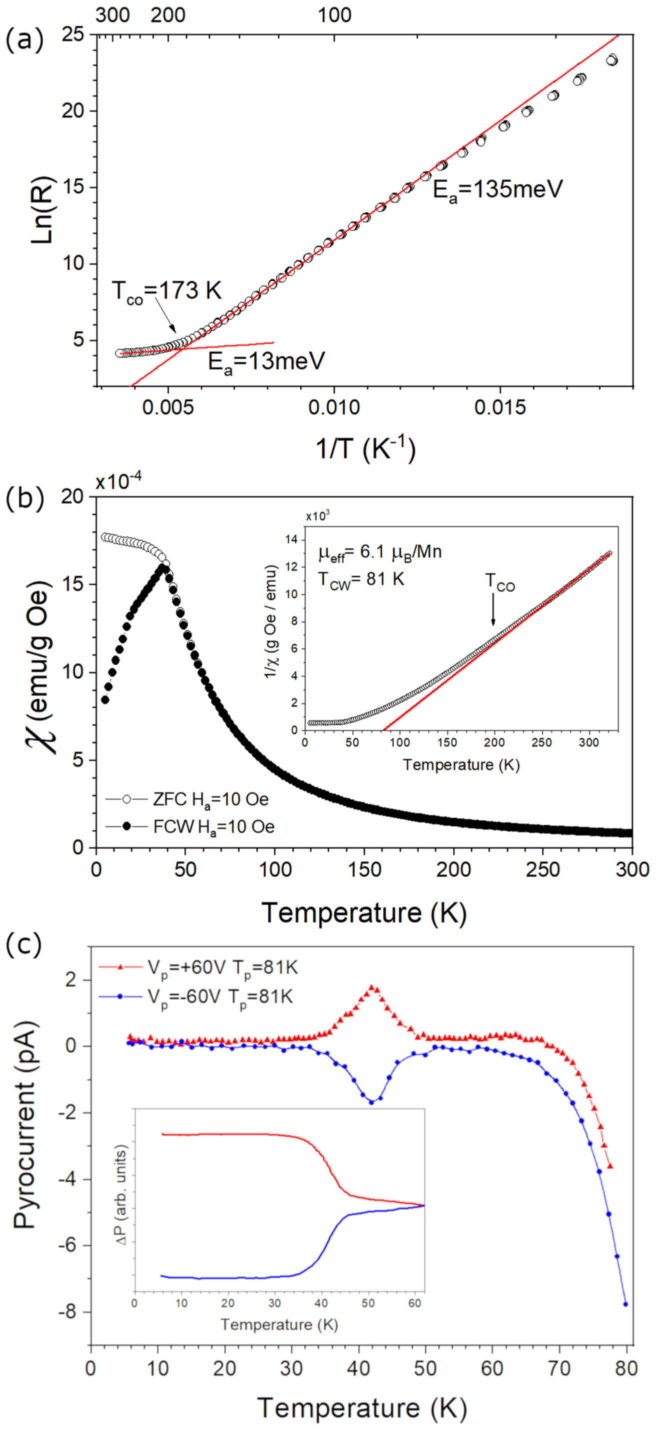

FIG. 1. (a) Electrical resistivity of the $Bi_{0.68}Ca_{0.32}MnO_3$ sample; the red lines correspond to the Arrhenius best fits. (b) ZFC and FCW curves measured by applying $H_a = 10$ Oe in the temperature range 2–300 K. The inset shows the inverse susceptibility, where the red line represents the best linear fit at high temperature. (c) Pyrocurrent measurements obtained by poling the sample at 81 K with ±60 V. The inset shows the integration of the pyrocurrent from 5 to 60 K. An Arrhenius plot of the high-temperature conductive tail yields activation energy $E_a = 122$ meV (not shown in the figure).

behavior in the transport properties is usually related to the CO transition in which the localization of the Mn e_g electron induces the insulating state [61].

The $Bi_{0.68}Ca_{0.32}MnO_3$ magnetization measurements [Fig. 1(b)] show a clear bifurcation between ZFC and FCW measurements around ≈45 K. The irreversibility of the two curves suggests the presence of ferromagnetic correlations. The inverse susceptibility of the sample, showing a clear deviation from linearity starting at ≈175 K in correspondence with the CO transition temperature, is reported in the inset of Fig. 1(b). The Curie-Weiss fit of the high-temperature region returned a positive Curie-Weiss temperature and a μ_{eff} value of $6.1\mu_B$ indicating the likely formation of ferromagnetic Mn—Mn pairs already in the paramagnetic region as observed in previous reports [45,46] as well as in $Bi_{0.75}Sr_{0.25}MnO_3$ [39].

Below T_{CO}, and in particular below 90 K, the insulating properties of $Bi_{0.68}Ca_{0.32}MnO_3$ allow us to perform pyrocurrent measurements obtained by poling the sample at $T_p =$ 81 K. The results of the pyrocurrent characterizations obtained in both poling field polarities (V_p +60 and −60 V, respectively) are reported in Fig. 1(c). A broad peak, centered at 42 K, is observed in the measurements indicating a change in the system polarization in correspondence with the magnetic transition observed in the ZFC and FCW measurement. The prominent negative pyrocurrent signal above 70 K is related to the rapid increase of the sample conductivity. This is also confirmed by the activation energy of the conductive tail that is 122 meV in agreement with the resistivity measurements. The observation of a clear pyrocurrent signal at the magnetic transition temperature indicates a change of the polarization but not strictly a ferroelectric transition, as will be discussed later.

B. Charge-ordered phase

At high temperature $Bi_{0.68}Ca_{0.32}MnO_3$ presents the classical $GdFeO_3$-type structure with strong octahedral tilting. The Rietveld refinement of the orthorhombic phase was performed against the TOF-NPD data at 200 K. Crystal data and refinement parameters are reported in Table SI [62] whereas atomic positions, anisotropic atomic displacement parameters (ADPs), and bond lengths are reported in Tables SII and SIII [62]. Figure 2 shows the Rietveld plot with the (ac)-projection of the structure showing the $a^-a^-c^+$ octahedra tilting [63] with a tilting angle $\phi_c = 26.03(14)^\circ$ along the c-axis and of $\phi_{ab} = 26.15(10)^\circ$ in the (ab)-plane. Bond distances unveil that the MnO_6 polyhedra are almost regular (see Table S II) [62], and bond valence sum (BVS) calculation returns a value of 3.316(5) for Mn in agreement with the expected composition.

To study the charge ordering below T_{CO}, we collected 3D-ED data on a microcrystal of $Bi_{0.68}Ca_{0.32}MnO_3$ at room temperature and 120 K. As will be discussed in detail in the next section, even if the data are collected below the magnetic long-range ordering transition, the possible induced distortions are not observed in the electron diffraction data. The 120 K 3D-ED data show additional reflections (selected reflections/rows have been highlighted by white arrows in Fig. 3) compared to the room-temperature dataset. These additional reflections can be indexed assuming a modulation vector $q = \frac{1}{2}a^* + \frac{1}{2}c^*$ with respect to the $Pbnm1'$ unit cell. The indexing of the electron diffraction data leads to a new orthorhombic unit cell with cell parameter $a = 15.61(1)$ Å,

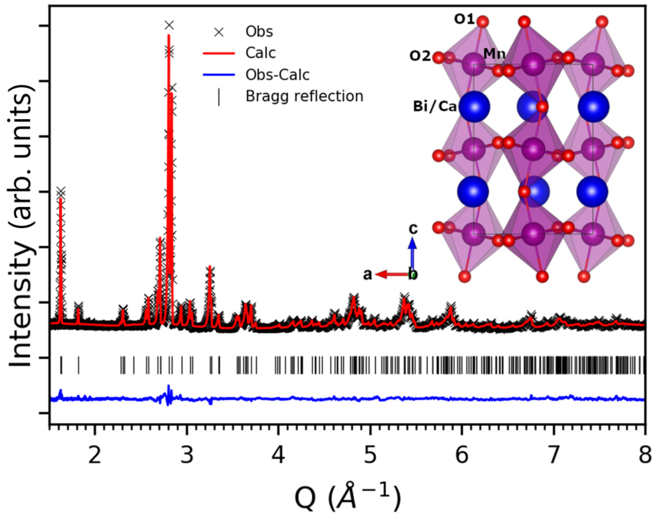

FIG. 2. Rietveld plot of the 200 K TOF-NPD data. Observed (black crosses), calculated (red line), and difference (blue line) patterns are reported; the black tick marks represent the Bragg positions. The inset shows the (*ac*) projection of the refined model, the violet polyhedra represent the MnO_6 octahedra, whereas blue spheres indicate the Bi/Ca site. The reliability factors are GOF = 2.11 $R_p =$ 0.0198 and $R_{wp} = 0.0251$.

$b = 10.94(1)$ Å, $c = 5.54(1)$ Å. The same unit cell was reported by García-Muñoz *et al.* [47,48] but it was related to the presence of two independent propagation vectors $q_1 = \frac{1}{2}a^*$ and $q_2 = \frac{1}{2}c^*$ in contrast with our observation. Given the presence of a shadow cone in the electron data, intrinsically due to the limited tilting range of the TEM sample holder, the extinction conditions could not be definitively determined. The systematic absences precisely determined are the following: hkl with $h + k = 2n$ and $0kl$ with $k = 2n$. This leads to the extinction classes *C--(a,b)*, *C-c-*, *C-c(a,b)*, and *C---*.

The possible isotropy subgroups deriving from the action of the modulation vector q on the parent $Pbnm1'$ structure were obtained with the ISODISTORT software [56–58] accounting only for an order/disorder distortion on the Mn site. Two irreducible representations (irreps), T_1 and T_2, return a $Cmc2_11'$ orthorhombic structure consistent with the observed systematic absences in the electron diffraction data. Both subgroups are defined in the same unit cell related to the parent $Pbnm1'$ structure by the transformation matrix {(0, 0, 2), (2, 0, 0), (0, 1, 0)} but with two different origin choices: $(\frac{1}{4}, 0, \frac{1}{4})$ and $(\frac{3}{4}, 0, \frac{1}{4})$ for T_1 and T_2, respectively. Even if the two subgroups are defined by the same space group in the same unit cell, the two different origin choices make them nonequivalent, and a careful evaluation of both against the diffraction data is required. Indeed, the two different origin choices will correspond to a different superposition of the symmetry breaking distortion with the preexisting ones, as shown, for example, in $BiFe_{0.5}Sc_{0.5}O_3$ [64,65] or in CeSbTe [66] for a nuclear and magnetic distortion, respectively. In the present case, the two origin choices determine the arrangement of the CO pattern with respect to the $a^-a^-c^+$ octahedra tilting as shown in Fig. 4, in which the charge ordered structure in the (*ab*)- and (*bc*)-plane is shown. The differently colored octahedra indicate the two independent crystallographic sites, Mn1 and Mn2, organized in stripes in the (*bc*)-plane. Along the *a*-axis (*c*-axis of the parent $Pbnm1'$ structure), clusters of four symmetry equivalent octahedra are arranged in a chesslike motif. As is highlighted by the red squares in Figs. 4(c) and 4(d), the four symmetry equivalent site are grouped around an *A*-site coordination polyhedron (highlighted in light blue in Fig. 4) elongated along the *b*-axis in the case of the T_1 irrep, whereas in the case of the T_2 irrep they are arranged around an *A*-site polyhedron elongated along the *a* direction. This will lead to different local environments for the two symmetry independent Mn sites,

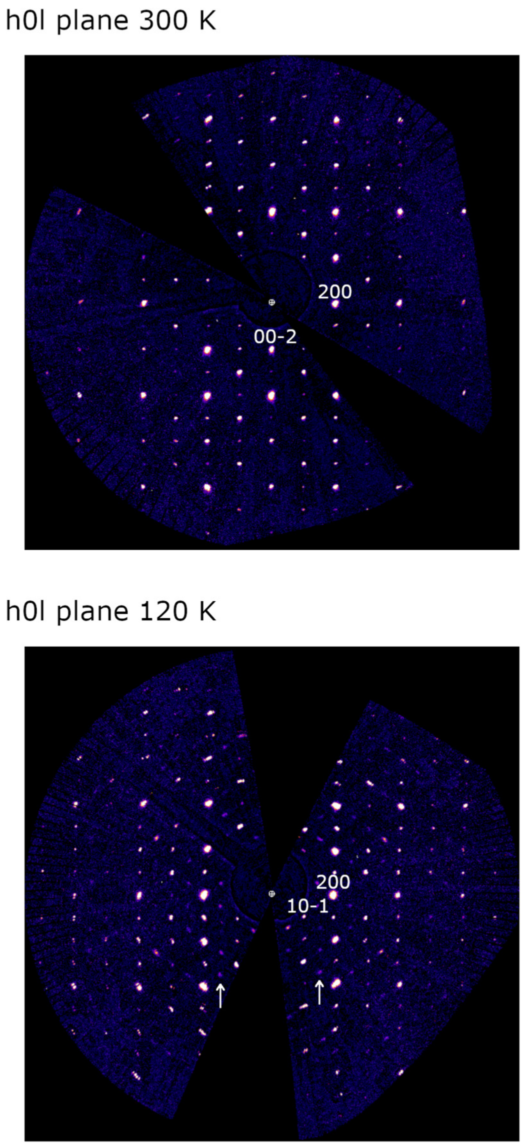

FIG. 3. Section across the $h0l$ plane of the three-dimensional reconstruction of the reciprocal space obtained with 3D-ED at 300 and 120 K. The missing areas are due to the beam stop shadow and to the part of the reciprocal space not reachable because of geometrical experimental constraints (limited tilting range). The reflections are indexed according to the $Pbnm1'$ unit cell; the white arrows at 120 K indicate the rows of additional reflections with modulation vector $q = \frac{1}{2}a^* + \frac{1}{2}c^*$ absent in the 300 K data. A selection of other sections is shown in Fig. S1 [62].

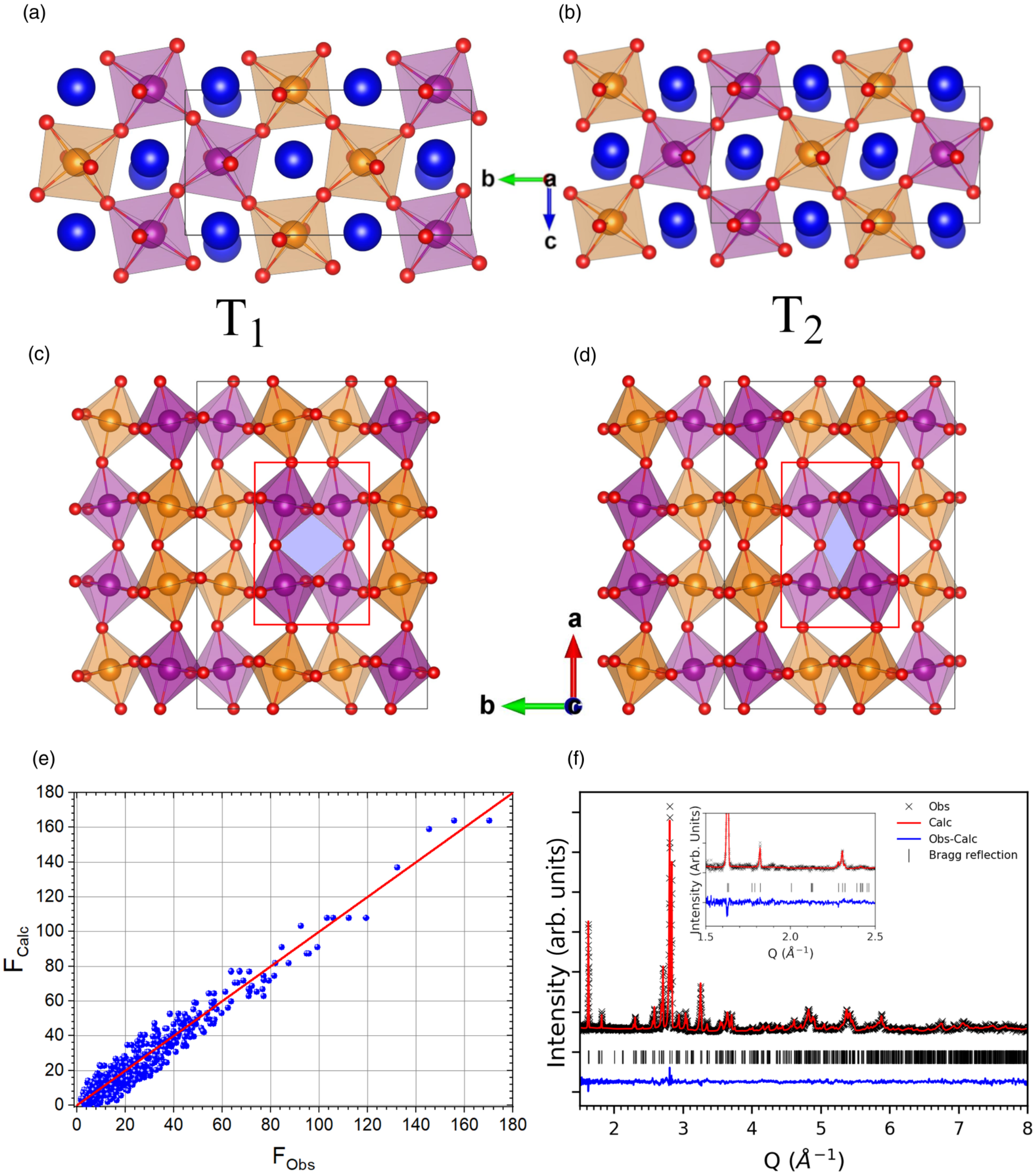

FIG. 4. (a)–(d) Sketch of the charge ordered structure in the (bc)- and (ab)-plane for the T_1 (a), (c) and T_2 (b), (d) models. The violet polyhedra represent the Mn1O$_6$ octahedra, whereas the Mn2O$_6$ octahedra are reported in orange. The blue spheres indicate the Bi/Ca site, which are omitted for clarity in panels (c), (d). The red squares in (c) and (d) focus on the different arrangements between the CO pattern and the octahedral tilting of the parent $Pbnm1'$ structure. The light blue regions highlight the A-site polyhedron. (e) Calculated structure factors (F_{calc}) against observed structure factor (F_{obs}) of the T_1 model for the combined refinement of the electron diffraction data collected at 120 K. The reliability factor are GOF = 4.95, $R_{(\text{obs})} = 0.185$, and $R_{\text{wp}} = 0.167$. (f) Rietveld plot of the 120 K TOF-NPD data. Observed (black crosses), calculated (red line), and difference (blue line) patterns are reported together with the Bragg positions of the CO phase (black tick marks). The inset represents a zoom of the low Q region showing that there is not an overestimation of the superstructural CO peaks. The neutron reliability factors are GOF = 1.24, $R_p = 0.0322$, and $R_{\text{wp}} = 0.0375$. The overall goodness of fit for both electron and neutron data is GOF$_{\text{overall}} = 2.56$.

and as consequence different Mn—O bond lengths in the two cases.

The refinement of the 3D-ED data has been performed for both subgroups assuming kinematic intensities, which is an approximation since the combination of 3D-ED geometry and precession electron diffraction allows only to mitigate the dynamical effects. The simultaneous refinement of the TOF-NPD data allows us to constrain the average structure and avoid misinterpretation of the 3D-ED data due to the latter approximation. During the refinement, reflections strongly affected by dynamical effects were excluded from the refinement following the criteria $|F_{\text{calc}} - F_{\text{obs}}| > 15\sigma(F_{\text{obs}})$. The least-squares refinements indicate a slight preference for the T_1 solution with an R value for the electron diffraction data

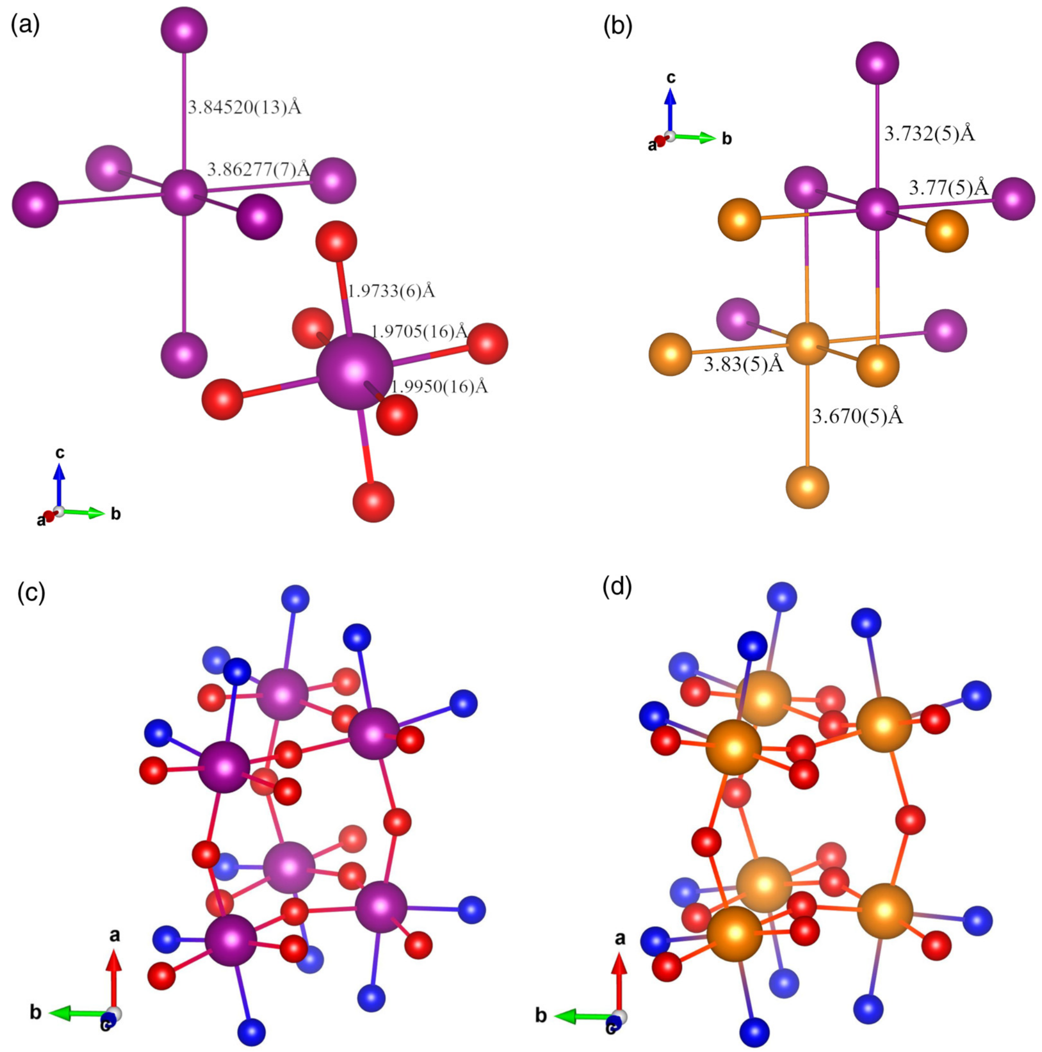

FIG. 5. (a) Geometry and selected distances for Mn—Mn and Mn—O in the high temperature $Pbnm1'$ structure. (b) Geometry and Mn—Mn distances in the CO T_1 model. Mn1 and Mn2 sites are reported in violet and orange, respectively. For clarity only the short Mn1—Mn1 and Mn2—Mn2 short distances described in the text are indicated. (c), (d) Arrangement of the short (with the red O sphere) and long (with the blue O sphere) Mn—O bonds, suggesting a change of the orbital state below T_{CO} for (c) Mn1 and (d) Mn2.

of 0.185 against 0.20 for the T_2 solution. On the contrary, the R_P values for the NPD data are equivalent for the two solutions (0.0322 versus 0.0323) as expected since the information regarding the CO resides in the electron diffraction data. The difference in the reliability factors between the two solutions is not large enough to unambiguously determine the CO structure, and detailed DFT calculations are needed [65]. For the purpose of this work, given the better reliability factors against the electron data, we will use the T_1 solution as our proposed model in the remainder of the paper. Nevertheless, we report the crystal data and the reliability factors for both solutions in Tables S IV and S VII, whereas atomic positions and a selection of bond lengths are reported in Tables S V–S IX in the Supplemental Material [62]. The good agreement between the observed and the calculated data is shown in Figs. 4(e) and 4(f) for both electron and neutron data.

The refined structure does not indicate a traditional CO between the two Mn sites. Indeed, the average Mn—O bond lengths are the same between the two sites within error [1.978(8) Å for the Mn1 site and 1.983(8) Å for the Mn2], and BVS calculations return the value of 3.39(15) and 3.35(15) for Mn1 and Mn2, respectively, in agreement with the value obtained in the $Pbnm1'$ phase. On the contrary, in the CO structure there is a clear change in the Mn—Mn distances. In the high-temperature charge disordered phase, the Mn—Mn distances are all almost equivalent with four equatorial ones of 3.862 77(7) Å and two axial ones of 3.845 20(13) Å, as shown in Fig. 5(a). At 120 K, the Mn1 sites are connected to equivalent Mn1 atoms via a short axial distance of 3.732(5) Å and two short equatorial ones of 3.77(5) Å [see Fig. 5(b)], whereas it shows longer distances with the Mn2 site: 3.91(5), 3.95(5), and 3.993(5) Å. The Mn2-Mn2 distances also reveal a similar distortion with a short axial distance of 3.670(5) Å and two short equatorial ones of 3.83(5) Å [see Fig. 5(b)], while Mn2-Mn1 distances are longer: 3.91(5), 3.95(5), and 3.993(5) Å. The formation of these short Mn—Mn distances points toward the formation of extended orbital molecules in $Bi_{0.68}Ca_{0.32}MnO_3$, as opposed to a classical Anderson charge localization [67]. The clustering of the Mn sites is also accompanied by a shortening of selected Mn—O bonds, as schematically shown in Figs. 5(c) and 5(d). Both Mn sites form four short bonds (Mn—O < 1.97 Å) and two long bonds (Mn—O > 2.0 Å), reinforcing the observation of "orbital molecules" in $Bi_{0.68}Ca_{0.32}MnO_3$.

C. Magnetic ordering

The magnetic structure of $Bi_{0.68}Ca_{0.32}MnO_3$ has been determined on the basis of the TOF-NPD data. On cooling below 150 K, the rise of new reflections is observed in the long d-spacing region (see Fig. S2) [62]. These extra reflections can be indexed with two propagation vectors $k_1 = (\frac{1}{2}\,0\,0)$ and $k_2 = (\frac{1}{2}\,\frac{1}{2}\,0)$ corresponding to the Z and U point of the first Brillouin zone of the parent $Pbnm1'$ structure. It is worth emphasizing that these extra reflections have a broad Lorentzian profile indicating a shorter correlation length with respect to the nuclear domains. The symmetry analysis to determine the possible magnetic space groups has been performed considering the $Pbnm1'$ model as a parent structure. The best agreement between the observed and calculated data has been obtained for the P_a2_1/m magnetic space group as shown for the magnetic-only pattern in Fig. 6(a) and by the reliability factors reported in Table S X [62]. The P_a2_1/m magnetic space group corresponds to the action of the $mU_2^-U_3^-$ and mZ_1 irreps. If the CO distortions are taken into account, the magnetic space group is then reduced to P_Cm described in a unit cell with all directions doubled with respect to the $Pbnm1'$ model. The two magnetic order parameters can induce a nuclear distortion with propagation vector $k = (0\,\frac{1}{2}\,0)$, but we do not observe these types of reflections in the 3D-ED data collected at 120 K as shown by Fig. S3 [62] indicating that the magnetoelastic coupling can be considered null at least within the sensibility of our 3D-ED data. In the final refinement, the moment on all the Mn sites has been constrained to the same value. The magnetic ordering is a pseudo-CE antiferromagnetic structure [21,22] with the Mn moment aligned with the c axis of the parent $Pbnm1'$ structure. The ordered moment is strongly reduced, $1.720(6)\mu_B$, from the expected $3.7\mu_B$. The reduced moment and the broad Lorentzian shape of the magnetic reflections suggest the presence of frustration in the system. It is worth emphasizing that the CO order parameter and the magnetic one do not couple directly, which indicates the lack of a clear symmetry relation between them. As consequence, there is no phenomenological reason indicating that the CO structure drives the selection of the long-range magnetic state. These observations suggest that the magnetic and charge degree of freedom might be in competition as observed in related systems [37].

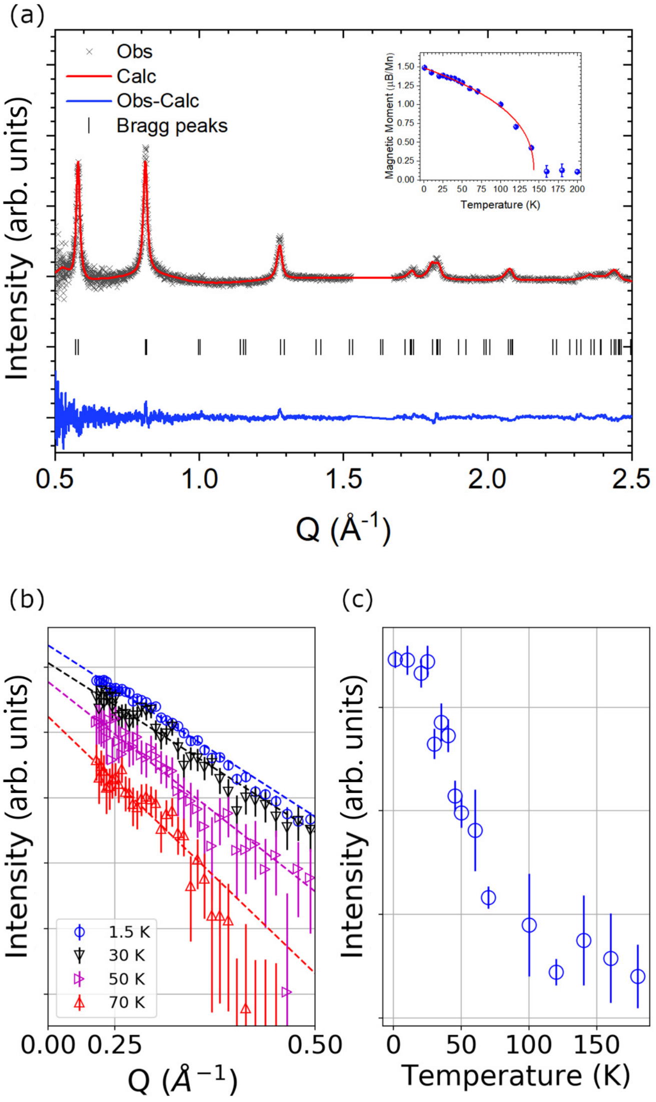

FIG. 6. (a) Rietveld plot of the TOF-NPD magnetic-only diffraction pattern, obtained subtracting the 200 K pattern from the 1.5 K one, collected at average $2\theta = 58.3^\circ$. Observed (black crosses), calculated (red line), and difference (blue line) patterns are reported; the black tick marks represent the Bragg positions. The refinement reliability factors are GOF = 1.12, $R_p = 0.0192$, and $R_{wp} = 0.0125$. The omitted region is due to the presence of a nuclear peak for which subtraction was not ideal due to the change in lattice parameters between 200 and 1.5 K. The inset shows the temperature evolution of the refined magnetic moment, and the red line represents the best fit with a power law $m_{Mn} = m_0(T - T_N)^\beta$. The fit returns a transition temperature $T_N = 143(2)$ K. (b) Low Q-region of the TOF-NPD data collected at average $2\theta = 27.08^\circ$ showing the scattering increase at low temperature. The data are shown in a $\ln(I)$ vs Q^2 scale allowing a better evaluation of the fit. The dashed lines represent the best fit of the data with a Guinier law $I(Q) = I_0 \exp(\frac{-(R_G^2 Q^2)}{3})$ where R_G is the gyration radius. (c) Temperature evolution of the I_0 parameter showing a sharp transition at ≈50 K in agreement with the magnetization data shown in Fig. 1(b).

Below 50 K, in correspondence with the divergence between ZFC and FC measurements as well as the peak in the pyrocurrent measurements [see Figs. 1(b) and 1(c)], a clear change in the low-Q background has been observed as shown in Fig. 6(b) and in Figs. S4 and S5 [62]. In particular, a strong increase of the scattering has been observed at low Q-values with a concomitant decrease at high Q suggesting the rise of ferromagnetic short-range correlations in the material (see Fig. S4) [62]. These correlations and the coexistence with the long-range AFM ordering were also observed in previous reports for composition in the low doping region of $Bi_{1-x}Ca_xMnO_3$ [46–48] as well as in other manganite systems [21,68,69]. To obtain qualitative information about the short-range correlations, a fit of the low Q-region of the TOF-NPD data with a Guinier law [70] has been performed.

It is worth emphasizing that the fit aims to highlight a qualitative evolution of the diffuse scattering and not to obtain precise information about shape, dimension, and dispersion of the ferromagnetic cluster/correlation. To obtain more quantitative results, data at lower Q are needed. Figure 6(b) shows the results of the fit against the TOF-NPD data after subtraction of the 200 K data to eliminate the instrumental scattering contribution at low Q (for comparison, the "raw" data are reported in Fig. S45 [62]). It is clear from the temperature evolution of the scattered intensity at $Q = 0$ [see Fig. 6(c)] that the diffuse scattering starts to be evident at ≈50 K and its intensity grows following a power law. From the Guinier fit, we obtain a temperature-independent gyration radius $R_G = 5.61(8)$ Å [70] as shown in Fig. S6 [62], which, assuming spherical correlation clusters, returns a volume of 1590(20) Å^3 corresponding to ≈7 times the cell volume of the parent $Pbnm1'$ structure. To draw a comparison with the work of Giot *et al.* [46], where a similar analysis of the diffuse scattering has been performed, we observed a significantly larger cluster size and a sharper transition at ≈50 K. Moreover, contrary to the latter work, we did not observe any obvious long-range ferromagnetic contributions.

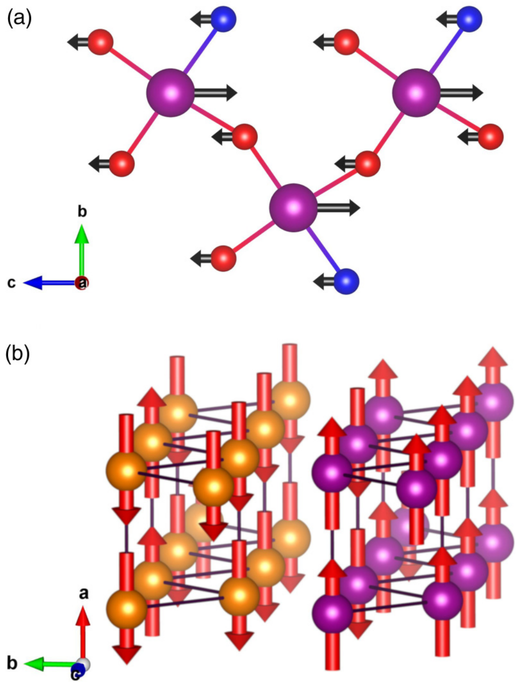

FIG. 7. (a) Drawing of the Γ_3^- distortion acting on the Mn (violet sphere) and O sites. O atoms involved in short Mn—O bonds are represented in red and O atoms involved in long Mn—O bonds are represented in blue. (b) Drawing of the pseudo-CE magnetic structure and of the clustering of the Mn cation (violet and orange spheres for Mn1 and Mn2, respectively) on the two independent sites due to the Γ_3^- and T_1 distortions. The black lines indicate the short distances between Mn ions, the formation of ferromagnetic dimers along the *a*-axis, and the extended zigzag "orbital molecules" along the *c*-direction.

IV. DISCUSSION

The possible occurrence of CO-induced polarization in manganites stimulated a controversial debate in the literature [3,23–27]. The typical finite conductivity of such materials, as well as frequent electric loss phenomena, have represented an objective drawback for the experimental validation of the predicted electric dipole ordering in CO phases [25–27]. In this scenario, a careful symmetry analysis of the CO transition could provide valuable insights concerning the potential spontaneous polarization in these systems allowing us to identify the secondary order parameters causing it. In the following, we apply this formalism to the CO transition in $Bi_{0.68}Ca_{0.32}MnO_3$.

The refinement of the electron and neutron diffraction data suggests the $Cmc2_11'$ space group with the origin at $(\frac{1}{4}, 0, \frac{1}{4})$, due to the action of the T_1 irreducible representation, as the best symmetry to describe the CO state. The two-dimensional T_1 order-disorder distortion, described by the scalar (σ_1, σ_2) order parameter, will couple the noncentrosymmetric one-dimensional Γ_3^- displacive distortion and the Γ_3^+ strain, described by the η and ϵ order parameters, respectively. Considering these three order parameters, it is possible to write the symmetry adapted free energy up to the fourth degree in σ_i:

$$F(\sigma_i, \eta, \epsilon) = \frac{a_0(T - T_{\mathrm{CO}})}{2}\left(\sigma_1^2 + \sigma_2^2\right) + b_1\left(\eta\sigma_1^2 - \eta\sigma_2^2\right) + c_1(\epsilon\sigma_1\sigma_2) + \frac{d_1}{4}\left(\sigma_1^4 + \sigma_2^4\right), \quad (1)$$

where a_0, b_1, c_1, and d_1 are phenomenological constants [71,72].

The second term of the expansion represents the linear quadratic coupling between the CO order parameter σ_i and the ferroelectric order parameter η. Instead, the third term describes the coupling between the CO and the Γ_3^+ strain. From the thermodynamic potential, we obtain three distinct phases by considering the different primary order parameter directions. If the general direction $\sigma_1 \neq \sigma_2 \neq 0$ is considered, both coupling terms are allowed, indicating that the CO induce both the ferroelectric and the elastic strain distortions, resulting in the $P2_11'$ space group. If $\sigma_1 = \sigma_2 \neq 0$, the coupling between the ferroelectric distortion and the CO vanishes, and the resulting phase has $P2_1/c$ symmetry. The last possible phase is when $\sigma_1 \neq 0$ and $\sigma_2 = 0$. In this case, the $\epsilon\sigma_1\sigma_2$ invariant vanishes and the second term reduces to $\eta\sigma_1^2$. The latter phase corresponds to the $Cmc2_1$ phase we determined as the best model from the electron and neutron diffraction measurements. This phase is an improper ferroelectric state, in which the free-energy invariant $\eta\sigma_1^2$ couples the CO order parameter with the induced ferroelectric distortion. Figure 7(a) shows the action of the Γ_3^- distortion along the polar axis acting on the Mn and O2 positions of the parent $Pbnm1'$ structure.

To evaluate the magnitude of these distortions, we performed a mode decomposition analysis of the experimental structure obtained from the electron and neutron data taking the 200 K $Pbnm1'$ structure as the parent. The results, reported in Table I, indicate a finite value for the Γ_3^- Au$_1$, A_1', and A_1 polar distortion modes for the Mn, O1, and O2 atoms, respectively, with amplitudes of −0.352 30, −0.645 16, and −0.744 96. The common action of these distortion modes

TABLE I. Results of the mode decomposition analysis performed on the refined CO structure at 120 K and using the 200 K refined structure as the parent. The table reports the irreducible representation and propagation vector, the order parameter direction, and the amplitude of the different modes for each site of the parent $Pbnm1'$ structure.

Irreducible representation and **k**	order parameter direction	Bi (mode)	Mn (mode)	O1 (mode)	O2 (mode)
Γ_1^+ (0,0,0)	(γ)	$0.07355(A_1')$		$0.13532(A_1')$	$-0.13473(A_1)$
		$0.05483(A_2')$		$-0.03028(A_2')$	$-0.00557(A_2)$
					$0.02948(A_3)$
Γ_3^- (0,0,0)	(η)	$-0.02452(A_1')$	$-0.35230(\mathrm{Au}_1)$	$-0.64516(A_1')$	$-0.74496(A_1)$
		$-0.02453(A_2')$	$0.20577(\mathrm{Au}_2)$	$0.01020(A_2')$	$-0.22127(A_2)$
			$-0.12341(\mathrm{Au}_3)$		$0.06074(A_3)$
T_1 (1/2,0,1/2)	$(\sigma_1, 0)$	$-0.05356(A_1')$	$-0.03617(\mathrm{Au}_1)$	$0.08146(A_1')$	$0.01686(A_1)$
		$-0.02838(A_2')$	$-0.04368(\mathrm{Au}_2)$	$0.13539(A_2')$	$-0.21166(A_2)$
		$0.08982(A'')$	$-0.05578(\mathrm{Au}_3)$	$-0.07718(A'')$	$0.02336(A_3)$
					$0.18715(A_4)$
					$-0.08120(A_5)$
					$-0.16840(A_6)$

gives rise to the spontaneous polarization. On the contrary, the Bi/Ca site does not show any particular polar distortion with the amplitude of the polar Γ_3^- modes an order of magnitude smaller than the Mn and O sites (see Table I). Unfortunately, as stated before, the transport properties of the sample at T_{CO} prevent a reliable measurement of the induced electrical polarization. Nevertheless, the pyroelectric measurements shown in Fig. 1(c) indicate a change of the spontaneous electrical polarization at the second magnetic transition temperature. Since the breaking of the spatial inversion symmetry occurs at T_{CO}, the evidence of a change in the spontaneous electrical polarization at 45 K indicates a renormalization of the spontaneous polarization already present in the system, endorsing the breaking of inversion symmetry at T_{CO}.

Some characteristics of the CO observed in $\mathrm{Bi_{0.68}Ca_{0.32}MnO_3}$ preclude a straightforward comparison with the traditional half-doped manganites. For instance, the ratio between $\mathrm{Mn^{3+}/Mn^{4+}}$ falls far from the 50/50 ratio, and moreover, the presence of the lone pair active $\mathrm{Bi^{3+}}$ determines local distortions that might promote or compete with Jahn-Teller instabilities and CO [31,32]. In a pure Anderson model (minimization of the Coulomb interaction) [67] applied to a scenario consisting of fully localized charges, one should expect a charge pattern that maximizes the number of bonds between the $\mathrm{Mn^{3+}}$ and $\mathrm{Mn^{4+}}$ cations. Instead, the observed stripe/chess-like structure seems to indicate that other interactions are involved in determining the system ground state. The mode decomposition analysis indicates the presence of antipolar displacive distortions with the T_1 and Γ_3^- symmetry acting on the Mn and O sites with comparable amplitudes with respect to the polar Γ_3^- modes. The Γ_3^- $\mathrm{Au_2}$ and $\mathrm{Au_3}$ Mn modes are responsible for the formation of the short Mn—Mn distances along the *c*-axis and in the (*ab*) plane [see Fig. 7(b)]. The concomitant clustering of the Mn sites and the rearrangement of the Mn—O bond with the four short bonds in the direction of the short Mn—Mn distances, as shown in Figs. 5(c) and 5(d), point toward the formation of extended “orbital molecules” in $\mathrm{Bi_{0.68}Ca_{0.32}MnO_3}$. Careful theoretical calculations are needed to confirm and understand the orbital distributions within the clusters, but the possibility of extended 1D orbital chains can widen our knowledge of these complex orbital states and open up new interesting opportunities in the field of quantum materials [19].

V. CONCLUSION

The low-temperature structure of $\mathrm{Bi_{0.68}Ca_{0.32}MnO_3}$ has been refined against the electron and neutron data simultaneously in the $Cmc2_11'$ space group. The qualitative refinement indicates the formation of a stripe/chess-like pattern with the presence of extended “orbital molecules” as suggested by the short Mn—Mn distances and from the rearrangement of the Mn—O bonds. Symmetry analysis and mode decomposition of the ordered structure confirm these observations and underline the presence of a spontaneous electrical polarization as the secondary order parameter as confirmed by the pyrocurrent measurement. Finally, neutron diffraction data at low temperature indicate the coexistence of short-range ferromagnetic correlations on a length scale of ≈7 unit cells and a long-range CE-type antiferromagnetic structure with a strongly reduced moment. This study reveals a strong competition between the charge, orbital, and magnetic degrees of freedom in $\mathrm{Bi_{0.68}Ca_{0.32}MnO_3}$ and how it can can lead to peculiar new phases [19].

ACKNOWLEDGMENTS

The authors thank the Science and Technology Facilities Council (UK) for the provision of neutron beam-time on the WISH beamline. The authors thank Chiara Pernechele for the assistance with the collection of the magnetization data. This work has benefited from the framework of the COMP-HUB Initiative, funded by the Departments of Excellence program of the Italian Ministry for Education, University and Research (MIUR, 2018-2022).

[1] M. Imada, A. Fujimori, and Y. Tokura, Metal-insulator transitions, Rev. Mod. Phys. **70**, 1039 (1998).

[2] E. H. da Silva Neto, P. Aynajian, A. Frano, R. Comin, E. Schierle, E. Weschke, A. Gyenis, J. Wen, J. Schneeloch, Z. Xu, S. Ono, G. Gu, M. Le Tacon, and A. Yazdani, Ubiquitous interplay between charge ordering and high-temperature superconductivity in cuprates, Science **343**, 393 (2014).

[3] J. van den Brink and D. I. Khomskii, Multiferroicity due to charge ordering, J. Phys.: Condens. Matter **20**, 434217 (2008).

[4] E. J. W. Verwey, Electronic conduction of magnetite (Fe_3O_4) and its transition point at low temperatures, Nature (London) **144**, 327 (1939).

[5] E. J. Verwey, P. W. Haayman, and F. C. Romeijn, Physical properties and cation arrangement of oxides with spinel structures II. Electronic conductivity, J. Chem. Phys. **15**, 181 (1947).

[6] E. J. Verwey and P. W. Haayman, Electronic conductivity and transition point of magnetite (Fe_3O_4), Physica **8**, 979 (1941).

[7] M. Iizumi, T. F. Koetzle, G. Shirane, S. Chikazumi, M. Matsui, and S. Todo, Structure of magnetite (Fe_3O_4) below the Verwey transition temperature, Acta Crystallogr., Sect. B **38**, 2121 (1982).

[8] M. Iizumi and G. Shirane, Crystal symmetry of the low temperature phase of magnetite, Solid State Commun. **17**, 433 (1975).

[9] J. P. Wright, J. P. Attfield, and P. G. Radaelli, Long Range Charge Ordering in Magnetite Below the Verwey Transition, Phys. Rev. Lett. **87**, 266401 (2001).

[10] M. S. Senn, J. P. Wright, and J. P. Attfield, Charge order and three-site distortions in the Verwey structure of magnetite, Nature (London) **481**, 173 (2012).

[11] S. J. Cassidy, F. Orlandi, P. Manuel, and S. J. Clarke, Single phase charge ordered stoichiometric $CaFe_3O_5$ with commensurate and incommensurate trimeron ordering, Nat. Commun. **10**, 5475 (2019).

[12] K. H. Hong, A. M. Arevalo-Lopez, J. Cumby, C. Ritter, and J. P. Attfield, Long range electronic phase separation in $CaFe_3O_5$, Nat. Commun. **9**, 2975 (2018).

[13] S. V. Ovsyannikov, M. Bykov, E. Bykova, D. P. Kozlenko, A. A. Tsirlin, A. E. Karkin, V. V. Shchennikov, S. E. Kichanov, H. Gou, A. M. Abakumov, R. Egoavil, J. Verbeeck, C. McCammon, V. Dyadkin, D. Chernyshov, S. van Smaalen, and L. S. Dubrovinsky, Charge-ordering transition in iron oxide Fe_4O_5 involving competing dimer and trimer formation, Nat. Chem. **8**, 501 (2016).

[14] J. B. Goodenough, The two components of the crystallographic transition in VO_2, J. Solid State Chem. **3**, 490 (1971).

[15] Y. Horibe, M. Shingu, K. Kurushima, H. Ishibashi, N. Ikeda, K. Kato, Y. Motome, N. Furukawa, S. Mori, and T. Katsufuji, Spontaneous Formation of Vanadium Molecules in a Geometrically Frustrated Crystal: AlV_2O_4, Phys. Rev. Lett. **96**, 086406 (2006).

[16] P. G. Radaelli, Y. Horibe, M. J. Gutmann, H. Ishibashi, C. H. Chen, R. M. Ibberson, Y. Koyama, Y.-S. Hor, V. Kiryukhin, and S.-W. Cheong, Formation of isomorphic Ir^{3+} and Ir^{4+} octamers and spin dimerization in the spinel $CuIr_2S_4$, Nature (London) **416**, 155 (2002).

[17] S. O. Long, A. V. Powell, S. Hull, F. Orlandi, C. C. Tang, A. R. Supka, M. Fornari, and P. Vaqueiro, Jahn-Teller driven electronic instability in thermoelectric tetrahedrite, Adv. Funct. Mater. **30**, 1909409 (2020).

[18] J. P. Attfield, Orbital molecules in electronic materials, APL Mater. **3**, 041510 (2015).

[19] D. I. Khomskii and S. V. Streltsov, Orbital effects in solids: Basics, recent progress, and opportunities, Chem. Rev. (2020), doi: 10.1021/acs.chemrev.0c00579

[20] A. S. Botana, V. Pardo, D. Baldomir, A. V. Ushakov, and D. I. Khomskii, Electronic structure of V_4O_7: Charge ordering, metal-insulator transition, and magnetism, Phys. Rev. B **84**, 115138 (2011).

[21] E. O. Wollan and W. C. Koehler, Neutron diffraction study of the magnetic properties of the series of perovskite-type compounds $(1-x)$LaxCaMnO$_3$, Phys. Rev. **100**, 545 (1955).

[22] J. B. Goodenough, Theory of the role of covalence in the perovskite-type manganites [La, M(II)]MnO$_3$, Phys. Rev. **100**, 564 (1955).

[23] P. G. Radaelli, D. E. Cox, M. Marezio, and S.-W. Cheong, Charge, orbital, and magnetic ordering in $La_{0.5}Ca_{0.5}MnO_3$, Phys. Rev. B **55**, 3015 (1997).

[24] A. Daoud-Aladine, J. Rodríguez-Carvajal, L. Pinsard-Gaudart, M. T. Fernández-Díaz, and A. Revcolevschi, Zener Polaron Ordering in Half-Doped Manganites, Phys. Rev. Lett. **89**, 097205 (2002).

[25] D. V. Efremov, J. van den Brink, and D. I. Khomskii, Bond-versus site-centred ordering and possible ferroelectricity in manganites, Nat. Mater. **3**, 853 (2004).

[26] S. Mercone, A. Wahl, A. Pautrat, M. Pollet, and C. Simon, Anomaly in the dielectric response at the charge-orbital-ordering transition of $Pr_{0.67}Ca_{0.33}MnO_3$, Phys. Rev. B **69**, 174433 (2004).

[27] A. M. L. Lopes, J. P. Araújo, V. S. Amaral, J. G. Correia, Y. Tomioka, and Y. Tokura, New Phase Transition in the $Pr_{1-x}Ca_xMnO_3$ System: Evidence for Electrical Polarization in Charge Ordered Manganites, Phys. Rev. Lett. **100**, 155702 (2008).

[28] N. Mathur, Magnetic phases to order, Nature (London) **400**, 405 (1999).

[29] N. Mathur and P. Littlewood, The self-organised phases of manganites, Solid State Commun. **119**, 271 (2001).

[30] C. Israel, M. J. Calderón, and N. D. Mathur, The current spin on manganites, Mater. Today **10**, 24 (2007).

[31] D. D. Khalyavin, R. D. Johnson, F. Orlandi, P. G. Radaelli, P. Manuel, and A. A. Belik, Emergent helical texture of electric dipoles, Science **369**, 680 (2020).

[32] G. Calestani, F. Orlandi, F. Mezzadri, L. Righi, M. Merlini, and E. Gilioli, Structural evolution under pressure of BiMnO$_3$, Inorg. Chem. **53**, 8749 (2014).

[33] F. Mezzadri, G. Calestani, M. Calicchio, E. Gilioli, F. Bolzoni, R. Cabassi, M. Marezio, and A. Migliori, Synthesis and characterization of multiferroic $BiMn_7O_{12}$, Phys. Rev. B **79**, 100106(R) (2009).

[34] F. Mezzadri, M. Buzzi, C. Pernechele, G. Calestani, M. Solzi, A. Migliori, and E. Gilioli, Polymorphism and multiferroicity in $Bi_{1-x/3}(Mn_3^{III})(Mn_{4-x}^{III}Mn_x^{IV})O_{12}$, Chem. Mater. **23**, 3628 (2011).

[35] E. Montanari, G. Calestani, L. Righi, E. Gilioli, F. Bolzoni, K. S. Knight, and P. G. Radaelli, Structural anomalies at the magnetic transition in centrosymmetric BiMnO$_3$, Phys. Rev. B **75**, 220101(R) (2007).

[36] A. A. Belik, S. Iikubo, T. Yokosawa, K. Kodama, N. Igawa, S. Shamoto, M. Azuma, M. Takano, K. Kimoto, Y. Matsui, and E.

Takayama-Muromachi, Origin of the monoclinic-to-monoclinic phase transition and evidence for the centrosymmetric crystal structure of $BiMnO_3$, J. Am. Chem. Soc. **129**, 971 (2007).

[37] A. A. Belik, Y. Matsushita, and D. D. Khalyavin, Reentrant structural transitions and collapse of charge and orbital orders in quadruple perovskites, Angewand. Chem. Int. Ed. **56**, 10423 (2017).

[38] J. L. García-Muñoz, C. Frontera, M. Respaud, M. Giot, C. Ritter, and X. G. Capdevila, Magnetic properties of $Bi_{0.75}Sr_{0.25}MnO_3 x \approx 2/8, T_{CO} = 600$ K: Ferromagnetism and charge order, Phys. Rev. B **72**, 054432 (2005).

[39] C. Frontera, J. L. García-Muñoz, M. A. G. Aranda, M. Hervieu, C. Ritter, L. Mañosa, X. G. Capdevila, and A. Calleja, Charge and zener polaron order in $Bi_{0.75}Sr_{0.25}MnO_3$, Phys. Rev. B **68**, 134408 (2003).

[40] H. Woo, T. A. Tyson, M. Croft, S.-W. Cheong, and J. C. Woicik, Correlations between the magnetic and structural properties of Ca-doped $BiMnO_3$, Phys. Rev. B **63**, 134412 (2001).

[41] M. Giot, P. Beran, O. Pérez, S. Malo, M. Hervieu, B. Raveau, M. Nevriva, K. Knizek, and P. Roussel, $Bi_{1-x}Ca_xMnO_3$ (x=0.4 and 0.45): X-ray single-crystal and electron microscopy study, Chem. Mater. **18**, 3225 (2006).

[42] W. Bao, J. D. Axe, C. H. Chen, and S.-W. Cheong, Impact of Charge Ordering on Magnetic Correlations in Perovskite $(Bi, Ca)MnO_3$, Phys. Rev. Lett. **78**, 543 (1997).

[43] H. L. Liu, S. L. Cooper, and S.-W. Cheong, Optical Study of the Evolution of Charge and Spin Ordering in the Manganese Perovskite $Bi_{1-x}Ca_xMnO_3 (x > 0.5)$, Phys. Rev. Lett. **81**, 4684 (1998).

[44] Y. Murakami, D. Shindo, H. Chiba, M. Kikuchi, and Y. Syono, Observations of long-period structures associated with charge ordering in $Bi_{0.2}Ca_{0.8}MnO_3$, Phys. Rev. B **55**, 15043 (1997).

[45] I. M. O. Troyanchuk and A. Chobot, Magnetic phase diagram of the $Bi_{1-x}Ca_xMnO_3$ manganites, Phys. Solid State **44**, 2266 (2002).

[46] M. Giot, A. Pautrat, G. André, D. Saurel, M. Hervieu, and J. Rodriguez-Carvajal, Magnetic states and spin-glass properties in $Bi_{0.67}Ca_{0.33}MnO_3$: Macroscopic ac measurements and neutron scattering, Phys. Rev. B **77**, 134445 (2008).

[47] J. L. García-Muñoz, C. Frontera, M. Respaud, M. Giot, C. Ritter, and X. G. Capdevila, Magnetic and electronic properties of $Bi_{0.75}Ca_{0.25}MnO_3$, J. Phys.: Condens. Matter **19**, 406212 (2007).

[48] J. L. García-Muñoz and C. Frontera, Spin disorder and magnetic properties of $Bi_{3/4}Ca_{1/4}MnO_3$, J. Appl. Phys. **103**, 07F718 (2008).

[49] P. A. Midgley and A. S. Eggeman, Precession electron diffraction–a topical review, IUCrJ **2**, 126 (2015).

[50] M. Gemmi and A. E. Lanza, 3D electron diffraction techniques, Acta Crystallogr. Sect. B **75**, 495 (2019).

[51] R. Vincent and P. Midgley, Double conical beam-rocking system for measurement of integrated electron diffraction intensities, Ultramicroscopy **53**, 271 (1994).

[52] M. Gemmi, E. Mugnaioli, T. E. Gorelik, U. Kolb, L. Palatinus, P. Boullay, S. Hovmöller, and J. P. Abrahams, 3d electron diffraction: The nanocrystallography revolution, ACS Central Sci. **5**, 1315 (2019).

[53] L. Palatinus, P. Brázda, M. Jelínek, J. Hrdá, G. Steciuk, and M. Klementová, Specifics of the data processing of precession electron diffraction tomography data and their implementation in the program PETS2.0, Acta Crystallogr. Sect. B **75**, 512 (2019).

[54] L. C. Chapon, P. Manuel, P. G. Radaelli, C. Benson, L. Perrott, S. Ansell, N. J. Rhodes, D. Raspino, D. Duxbury, E. Spill, and J. Norris, WISH: The new powder and single crystal magnetic diffractometer on the second target station, Neutron News **22**, 22 (2011).

[55] V. Petříček, M. Dušek, and L. Palatinus, Crystallographic computing system JANA2006: General features, Z. Kristallogr.-Cryst. Mater. **229**, 345 (2014).

[56] B. J. Campbell, H. T. Stokes, D. E. Tanner, and D. M. Hatch, ISODISPLACE: A web-based tool for exploring structural distortions, J. Appl. Crystallogr. **39**, 607 (2006).

[57] H. T. Stokes, D. M. Hatch, and B. J. Campbell, ISOTROPY Software Suite.

[58] D. M. Hatch and H. T. Stokes, INVARIANTS: Program for obtaining a list of invariant polynomials of the order-parameter components associated with irreducible representations of a space group, J. Appl. Crystallogr. **36**, 951 (2003).

[59] C. Bucci and R. Fieschi, Ionic Thermoconductivity. Method for the Investigation of Polarization in Insulators, Phys. Rev. Lett. **12**, 16 (1964).

[60] C. Bucci, R. Fieschi, and G. Guidi, Ionic thermocurrents in dielectrics, Phys. Rev. **148**, 816 (1966).

[61] L. Righi, J. Gutiérrez, and J. M. Barandiarán, Structure, magnetic and transport properties in $La_{0.7-x}Bi_xCa_{0.3}MnO_3$ perovskites, J. Phys.: Condens. Matter **11**, 2831 (1999).

[62] See Supplemental Material at http://link.aps.org/supplemental/10.1103/PhysRevB.103.104105 for crystallographic tables and extra figures.

[63] A. M. Glazer, The classification of tilted octahedra in perovskites, Acta Crystallogr. Sect. B **28**, 3384 (1972).

[64] D. D. Khalyavin, A. N. Salak, N. M. Olekhnovich, A. V. Pushkarev, Y. V. Radyush, P. Manuel, I. P. Raevski, M. L. Zheludkevich, and M. G. S. Ferreira, Polar and antipolar polymorphs of metastable perovskite $BiFe_{0.5}Sc_{0.5}O_3$, Phys. Rev. B **89**, 174414 (2014).

[65] S. A. Prosandeev, D. D. Khalyavin, I. P. Raevski, A. N. Salak, N. M. Olekhnovich, A. V. Pushkarev, and Y. V. Radyush, Complex antipolar $\sqrt{2} \times 4 \times 2\sqrt{2}$ structure with *Pnma* symmetry in $BiFeO_3$ and $BiFe_{1/2}Sc_{1/2}O_3$: First-principles calculations, Phys. Rev. B **90**, 054110 (2014).

[66] L. M. Schoop, A. Topp, J. Lippmann, F. Orlandi, L. Müchler, M. G. Vergniory, Y. Sun, A. W. Rost, V. Duppel, M. Krivenkov, S. Sheoran, P. Manuel, A. Varykhalov, B. Yan, R. K. Kremer, C. R. Ast, and B. V. Lotsch, Tunable Weyl and Dirac states in the nonsymmorphic compound CeSbTe, Sci. Adv. **4**, eaar2317 (2018).

[67] P. W. Anderson, Ordering and antiferromagnetism in ferrites, Phys. Rev. **102**, 1008 (1956).

[68] V. B. Shenoy and C. N. R Rao, Electronic phase separation and other novel phenomena and properties exhibited by mixed-valent rare-earth manganites and related materials, Phil. Trans. R. Soc. A **366**, 63 (2008).

[69] P. M. Woodward, D. E. Cox, T. Vogt, C. N. R. Rao, and A. K. Cheetham, Effect of compositional fluctuations on the phase transitions in $(Nd_{1/2}Sr_{1/2})MnO_3$, Chem. Mater. **11**, 3528 (1999).

[70] A. Michels, A. Malyeyev, I. Titov, D. Honecker, R. Cubitt, E. Blackburn, and K. Suzuki, Magnetic Guinier law, IUCrJ **7**, 136 (2020).

[71] J. C. Toledano and P. Toledano, *The Landau Theory of Phase Transitions: Application to Structural, Incommensurate, Magnetic and Liquid Crystal Systems*, World Scientific Lecture Notes in Physics (World Scientific, Singapore, 1987).

[72] Y. A. Izyumov and V. N. Syromyatnikov, *Phase Transitions and Crystal Symmetry* (Springer, Dordrecht, 1990).